


RESEARCH ARTICLE

Numerical characterization of regenerative axons growing along a spherical multifunctional scaffold after spinal cord injury

Weiping Zhu *, Han Zhang, Xuning Chen, Kan Jin, Le Ning

Shanghai Institute of Applied Mathematics and Mechanics, Shanghai University, Shanghai, People's Republic of China

* wpzhu@shu.edu.cn



Abstract

Spinal cord injury (SCI) followed by extensive cell loss, inflammation, and scarring, often permanently damages neurological function. Biomaterial scaffolds are promising but currently have limited applicability in SCI because after entering the scaffold, regenerating axons tend to become trapped and rarely re-enter the host tissue, the reasons for which remain to be completely explored. Here, we propose a mathematical model and computer simulation for characterizing regenerative axons growing along a scaffold following SCI, and how their growth may be guided. The model assumed a solid, spherical, multifunctional, biomaterial scaffold, that would bridge the rostral and caudal stumps of a completely transected spinal cord in a rat model and would guide the rostral regenerative axons toward the caudal tissue. Other assumptions include the whole scaffold being coated with extracellular matrix components, and the caudal area being additionally seeded with chemoattractants. The chemical factors on and around the scaffold were formulated to several coupled variables, and the parameter values were derived from existing experimental data. Special attention was given to the effects of coating strength, seeding location, and seeding density, as well as the ramp slope of the scaffold, on axonal regeneration. In numerical simulations, a slimmer scaffold provided a small slope at the entry “on-ramp” area that improved the success rate of axonal regeneration. If success rates are high, an increased number of regenerative axons traverse through the narrow channels, causing congestion and lowering the growth rate. An increase in the number of severed axons (300–12000) did not significantly affect the growth rate, but it reduced the success rate of axonal regeneration. However, an increase in the seeding densities of the complexes on the whole scaffold, and that in the seeding densities of the chemoattractants on the caudal area, improved both the success and growth rates. However, an increase in the density of the complexes on the whole scaffold risks an over-eutrophic surface that harms axonal regeneration. Although theoretical predictions are yet to be validated directly by experiments, this theoretical tool can advance the treatment of SCI, and is also applicable to scaffolds with other architectures.

OPEN ACCESS

Citation: Zhu W, Zhang H, Chen X, Jin K, Ning L (2018) Numerical characterization of regenerative axons growing along a spherical multifunctional scaffold after spinal cord injury. PLoS ONE 13(10): e0205961. <https://doi.org/10.1371/journal.pone.0205961>

Editor: Michael G. Fehlings, University of Toronto, CANADA

Received: August 23, 2017

Accepted: October 4, 2018

Published: October 26, 2018

Copyright: © 2018 Zhu et al. This is an open access article distributed under the terms of the [Creative Commons Attribution License](https://creativecommons.org/licenses/by/4.0/), which permits unrestricted use, distribution, and reproduction in any medium, provided the original author and source are credited.

Data Availability Statement: All data generated or analysed during this study are included in this published article.

Funding: This work was supported by the National Natural Sciences Foundation of China Grant No. 31370940.

Competing interests: The authors have declared that no competing interests exist.

Introduction

Spinal cord injury (SCI) typically results in a permanent loss of neurological function below the level of the injury [1,2]. Recovery from SCI is poor owing to weak intrinsic growth capacity of axons and an inhibitory microenvironment, as well as a lack of suitable growth substrates and growth-stimulating factors, that limit axonal regeneration. Many efforts have been made to overcome these impediments [3,4,5,6,7], including implanting of cells [8,9] and/or biomaterials [10,11,12,13,14,15,16,17], delivery of growth factors and degradation of inhibitory matrix molecules [18,19,20,21,22,23,24,25], activation of an intrinsic growth program [26], and stabilization of growth cones and the axonal cytoskeleton [27]. Biomaterial scaffolds that can fill or bridge a lesion cavity, provide a substrate for cell seeding, offer physical guidance to regenerating axons or act as a vehicle for drug delivery are highly promising for cellular and molecular regenerative therapies [19]. However, the use of biomaterial scaffolds as a bridge for SCI repair is complicated; for instance, a popular biomaterial scaffold has tunnels/linear pores, which could guide regenerating axons along these tunnels [14,19]. However, significant congestion was observed at the entry points to the scaffold, which lowered the number of axons entering the pores [19]. If pores were coated or seeded with extracellular components (ECM) components [14] or cells [19], the axons were likely to enter the tunnels from both rostral and caudal ends, but became trapped within them [14], unless an additional injection of cells and/or growth factors close to either side of the bridge was administered [18,19], after which some of the trapped axons would be attracted to the injection site and re-enter host tissues [19]. These issues involve the architecture of the “on-ramp” and “off-ramp” parts of the bridge [3], and the concentration gradients of the molecules released from the cells around and seeded on the scaffold, and their influence on successful growth rates of regenerative axons have not yet been clarified. As an analytical tool, mathematics can be used to address many aspects of these issues, for example, the role of slopes at the on-ramp part of a scaffold. When a scaffold with linear pores is used, the axons whose growth cones face to the pores can easily enter the pores owing to the zero entry slope for them, whereas for axons beside the pores, an abrupt or infinite (mathematically) slope exists, which obstructs the axons and leads to congestion. Therefore, theoretical models which address the physical basis underlying the regulatory effect of ligand gradients on axonal growth cone motility are highly desirable, as they have been previously used for studying axonal growth during neural development [28,29,30,31]. Axonal growth or regrowth follow the same principle, both during development and following injury. A difference between them, however, has been observed in the level of factors present in their micro-environments [1,2]. Therefore, a theoretical model for axonal growth during development should be modified for studying SCI. Previously, in an initial study [32], we numerically demonstrated that SCI leaves a spherical glial scar. During therapeutic treatment with Schwann cell coating, regenerating axons were shown to grow across the scar and reach their target cells under certain conditions.

In this study, we assumed a solid, spherical, multifunctional, biomaterial scaffold that would bridge the rostral and caudal stumps of a completely transected spinal cord in a rat model and guide the regenerative rostral axons toward the caudal tissue (Fig 1). The rostral and caudal areas of the scaffold were referred to as the entry “on-ramp” area and the exit “off-ramp” area, respectively. The whole scaffold was coated with extracellular matrix components, and the caudal area (off-ramp) was additionally seeded with chemoattractants. In this context, the chemical factors on and around the scaffold were formulated to several coupled variables, and the parameter values were derived from existing experimental data. The effects of axonal regeneration on the on-ramp slope of the scaffold and biomedical modifications were numerically simulated to provide a quantitative interconnection between axonal regeneration and the

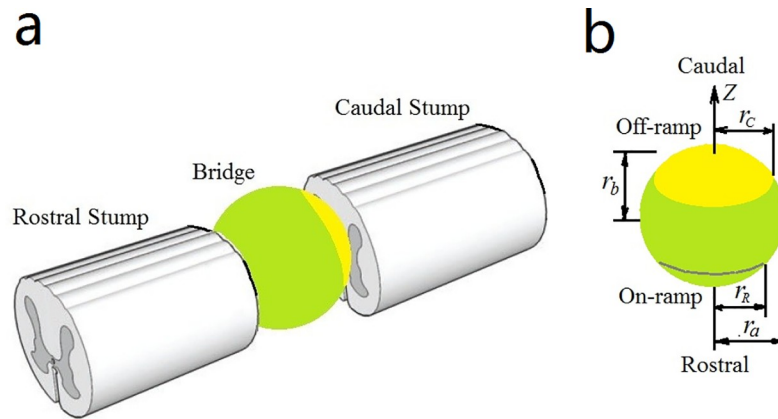


Fig 1. Schematics of an injured spinal cord bridged by a spherical scaffold. **a)** A complete transection of spinal cord with a gap bridged by a spherical scaffold between the rostral and caudal stumps. **b)** The scaffold architecture, coordinate system, and symbols employed in the mathematical models. The fabricated scaffold is assumed to be coated with hydroxylapatite (HA)/extracellular matrix (ECM) components (collagen I, fibronectin, and laminin I) and HA/LV-chondroitinase ABC (ChABC) over the whole surface (green). Additional HA/LV-NT-3/LV-brain-derived neurotrophic factor (BDNF) was coated on the off-ramp area (yellow).

<https://doi.org/10.1371/journal.pone.0205961.g001>

biophysical properties of the components for rational design of scaffolds in tissue engineering [33], as well as contribute to a better understanding of the biological processes involved. From this model and the simulations, we can learn what constitutes a good scaffold, good entry points for regenerative axons, and the resultant concentrations of the molecules from the microenvironment and the scaffold, and how the sources of the main attractants vary along the length of the scaffold in a monotonic curve. Moreover, our model can be modified to optimize scaffolds with other architectures, including differences in size and shape, in concentration of molecules inside and around the scaffold, and before and after experiments.

Materials and methods

Materials and methods have been described primarily from the computational point of view.

Geometry of the scaffold

The scaffold is assumed to be a rotational ellipsoid in such a coordinate system that the z -axis is the rotational axis and is orthogonal to the x - and y -axes (Fig 1B), and the origin $O(0, 0, 0)$ is at the ellipsoid center. The lateral and longitudinal semi-axes of the ellipsoid are denoted by r_a and r_b , respectively. When r_a and r_b are equal, the ellipsoid becomes a perfect sphere. Moreover, the rostral and caudal sides of the scaffold are defined as the entry on-ramp and exit off-ramp, respectively [3]. The longitudinal length of the on-ramp/off-ramp (measured from the scaffold end-point to where the rotational radius of the scaffold surface equals r_R/r_C) is $r_b/3$. The length parameters (r_a, r_b, r_C, r_R , and others) are scaled to dimensionless values by the characteristic length L of the model. The parameter r_a is controllable, and r_b is fixed at $2 \times r_b \times L = 3$ mm (spanning the gap of the spinal cord). Three scaffolds were prepared: slim ($r_a \times r_b = 0.15 \times 0.3$), round (0.3×0.3), and stocky (0.45×0.3), labeled as No. 1, No. 2, and No. 3, respectively. For brevity, all scaffolds are referred to as “spherical”, noting that when the longitudinal size r_b is fixed, the on-ramp/off-ramp slope is proportional to the lateral size r_a . Correspondingly, the entry slopes of the slim, round, and stocky scaffolds are small, medium, and large, respectively. Therefore, when studying the effect of the entry slope of the scaffold on axonal regeneration, we need to vary r_a in the model.

Assumptions about fabrication, coating, and seeds of the scaffold. In the current study, processing a scaffold relates to setting the model parameters. There are several existing techniques available for fabrication and modification of the scaffold, for example the poly (D,L-lactide-co-glycolide) (PLG) with a gas-foaming/particulate-leaching process [14,24]. To prepare the coating and seeds of the scaffold, hydroxylapatite (HA) nanoparticles (Sigma-Aldrich) were suspended in phosphate-buffered saline and sonicated for 1 min to dissociate the aggregates [14,24]. The nanoparticles were then complexed with several ECM components (forming HA/ECMs), including collagen I (BD Biosciences, San Jose, CA), fibronectin (Sigma-Aldrich, St. Louis, MO), and laminin I (Trevigen, Gaithersburg, MD) [22]. Lentivirus was used to encode the neurotrophic factors NT-3 (HA/LV-NT-3) and BDNF (HA/LV-BDNF) [24] and the ChABC gene (HA/LV-ChABC) [21,23,24]. The HA/ECMs and HA/virus complexes were then incubated for 10 min at 4°C and deposited onto the scaffold surface using Stripper pipette tips (Mid-Atlantic Diagnostics, Mount Laurel, NJ). The HA/ECMs and HA/LV-ChABC were coated over the entire surface, whereas HA/LV-NT-3 and HA/LV-BDNF were only deposited on the off-ramp surface of the bridge. Although HA could firm the coating and/or seeds on the PLG material surface [24], it probably stimulates bone formation [34]; therefore, it would be best to avoid the overuse of HA. In addition, the prepared scaffold should be placed on dry ice until implantation. This scaffold could then be used to replace previous scaffolds used in a rat model for SCI repair [10,11,16], to bridge a gap of approximately 3 mm. The scaffold was considered to perform the following functions: the factors seeded on the bridge surface were localized and sustained; the on-ramp slope introduced the rostral regenerative axons onto the scaffold; the secreted ChABC cleared the growth pathways; the ECM components kept the axons on target; and the gradients of the secreted NT-3 and BDNF guided the growing rostral axons along the correct path while blocking the caudal axons.

Scaffold surface equation and constraints for growth cones

Geometrically, the scaffold is an ellipsoid that rotates about its z-axis (Fig 1B). The surface equation reads as follows:

$$(R/r_a)^2 + (z/r_b)^2 = 1, \text{ with } R = \sqrt{x^2 + y^2}. \tag{1}$$

Here, x , y , and z are the coordinates of a point on the surface and R is the distance from that point to the z-axis.

When an axon grows along the scaffold surface, the growth cone can be considered as a particle moving on the surface. The ECM molecules coated on the scaffold are assumed to strongly adhere to the membrane proteins of the growth cones, tethering them to the scaffold. In other words, the movements of the growth cones are constrained by Eq (1). Taking the time derivative of both sides of Eq (1), the constraint conditions of the growth cone velocity can then be obtained as follows:

$$V_R = -(r_a/r_b)^2 V_z z/R, \quad V_R = dR/dt, \quad V_z = dz/dt, \tag{2}$$

$$V_x = dx/dt = V_R x/R, \quad V_y = dy/dt = V_R y/R, \tag{3}$$

where V_x , V_y , and V_z are the velocity components of a growth cone in the x -, y -, and z -directions, respectively, and V_R is the velocity component along the rotational radius R . In Eq (2), V_z is the longitudinal velocity of the growth cone, which defines the drawing speed or growth rate of the axons. When $V_z > 0$, the axon is elongating. Otherwise it is retracting. V_R is the lateral velocity of the growth cone. When $V_z > 0$ and $z < 0$, $V_R > 0$ and the growth cone progresses from the on-ramp of the scaffold. Conversely, when $V_z > 0$ and $z > 0$, $V_R < 0$ and the growth

cone advances to the off-ramp. In the next two subsections, we describe the drawing force and locomotive guidance of the growth cone along the scaffold.

Equations for axonal growth

Many pieces of evidence have shown that axonal growth cones move because of chemotactic processes, biased toward (attractive chemotaxis) or away from (repulsive chemotaxis) the chemical source [35,36,37]. The chemicals that attract and repel regenerative axons are found on and around the multifunctional scaffold (this is hereafter assumed to be the case in the implanted status), and will be classified in the next subsection. The chemotactic force, which defines the attractive or repulsive action on a growth cone, is proportional to the gradient of the diffusible molecules released from the chemical source [29,32,37,38,39,40,41]. The growth cone can be regarded as a particle whose persistent velocity determines the growth rate of an axon. As axonal growth is particularly slow (approximately $0.01 \mu\text{ms}^{-1}$) [35,36,37], the acceleration or inertial force can be neglected [24]. Stochastic factors can also be neglected because the chemotactic movement is highly consistent [29]. Therefore, the velocity of the growth cone is directly proportional to the chemotactic force:

$$\frac{d\mathbf{r}_k^A}{dt} = \frac{1}{\mu} \mathbf{F}_k^A, \quad k = 1, 2, \dots, N_A, \tag{4}$$

$$\mathbf{F}_k^A = \sum_{i=1}^3 \lambda_i \mathbf{p}_i, \quad \mathbf{p}_i = \nabla \rho_i \frac{|\Delta \mathbf{r}_k^A|}{\rho_\Sigma}, \quad \rho_\Sigma = \sum_{i=1}^3 \rho_i, \quad i = 1, 2, 3, \tag{5}$$

where k and N_A are the number and total number of regenerative axons/growth cones, respectively. $\mathbf{r}_k^A (= x_k^A \mathbf{i} + y_k^A \mathbf{j} + z_k^A \mathbf{k})$, where \mathbf{i} , \mathbf{j} , and \mathbf{k} are the unit vectors in the Cartesian coordinate system) is the position of the k -th growth cone at time t . μ is the dynamic viscosity coefficient. $\mathbf{F}_k^A (= F_{xk}^A \mathbf{i} + F_{yk}^A \mathbf{j} + F_{zk}^A \mathbf{k})$ is the result of the chemotactic forces from all types of chemotactic-related molecules (CRMs) acting on the k -th growth cone at t . The CRMs will be classified into three types in the next subsection, where i is the number of types of CRMs, and subscript i denotes the i -th type of CRMs (CRMs- i). The chemotactic force [Eq (5)] is defined as a dimensionless vector (\mathbf{p}_i) with a proportionality constant (λ_i). In this equation, ρ_i is the concentration of CRMs- i at \mathbf{r}_k^A and t ; $\nabla \rho_i$ is the gradient of ρ_i (where $\nabla = \mathbf{i}\partial/\partial x + \mathbf{j}\partial/\partial y + \mathbf{k}\partial/\partial z$ is the Hamiltonian operator); $|\Delta \mathbf{r}_k^A| = \sqrt{\Delta x^2 + \Delta y^2 + \Delta z^2}$ is the scalar difference of \mathbf{r}_k^A across the width of the k -th growth cone; and ρ_Σ is the sum of ρ_i over all types of CRMs. Note that the scalar of \mathbf{p}_i [Eq (5)] simplifies to $\Delta \rho_i / \rho_\Sigma$, which expresses the relative difference of ρ_i , with $\Delta \rho_i$ being the absolute difference of ρ_i across the distance $|\Delta \mathbf{r}_k^A|$. In practice, the average width of the growth cone can be considered as $|\Delta \mathbf{r}_k^A| \sim 10 \mu\text{m}$ [29,38]. Therefore, the gradient and relative difference of the chemotactic concentration are mathematically linked through \mathbf{p}_i . The corresponding proportionality constant λ_i then acquires a clear physical meaning of force per unit length. This model considerably reduces the growth-rate distortion of the growth cone when close to the target cells. Note that in the one-dimensional single-component problem [29,38,39], \mathbf{p}_i reduces to $p = \Delta \rho / \rho$, which defines the concentration gradient in some biophysical areas.

Finally, from Eqs (2), (4) and (5), the drawing speed V_z of the k -th axon can be expressed as follows:

$$V_{zk} = \frac{dz_k^A}{dt} = \frac{1}{\mu} F_{zk}^A, \quad k = 1, 2, \dots, N_A, \tag{6}$$

$$F_{zk}^A = \sum_{i=1}^3 \lambda_i \frac{\partial \rho_i}{\partial z} \cdot \frac{\Delta z}{\rho_\Sigma}, \quad \rho_\Sigma = \sum_{i=1}^3 \rho_i, \tag{7}$$

where Δz is the cone’s width along the z -axis. The other symbols have been defined in Eqs (4) and (5).

Evolution equations for the chemotactic-related molecules

Based on the chemical coarse-graining concept, the chemotactic-related molecules (CRMs) on and around the multifunctional scaffold can be classified into three types. The first group (denoted as Type 1 or CRMs-1) comprises the chemoattractants for axonal growth, such as NT-3 and BDNF [35,36], secreted by seeded HA/LV-NT-3 and HA/LV-BDNF at the off-ramp area (Fig 1B; yellow). The second group (Type 2 or CRMs-2) comprises the chemorepellents Nogo-60, myelin-associated glycoprotein (MAG), and oligodendrocyte-myelin glycoprotein (OMG) released or upregulated in response to the injured tissues [42,43,44,45]; and the remnant chondroitin sulfate proteoglycans (CSPGs) that are not neutralized by ChABC [1,2,9], secreted by seeded HA/LV-ChABC over the entire scaffold surface. Finally, the third group (Type 3 or CRMs-3) includes molecules released from coated HA/ECM components (collagen I, fibronectin, and laminin I) on the scaffold, which support axonal growth [24,35,36]. The mixed concentrations of CRMs-1, CRMs-2, and CRMs-3 are denoted by $\rho_1, \rho_2,$ and $\rho_3,$ respectively. Among these groups, CRMs-1 plays the leading role in promoting axonal regeneration, CRMs-2 inhibits axonal growth, and CRMs-3 plays a supplementary role in stabilizing axonal growth. In addition, CRMs-1 and CRMs-2/3 might crosstalk via signal transduction [46]. The diffusions and reactions of $\rho_1, \rho_2,$ and ρ_3 obey Fick’s first law [28,29]. Considering these CRM mechanisms in SCI regeneration, the evolution equations for $\rho_1, \rho_2,$ and ρ_3 are given as follows:

$$\frac{\partial \rho_1}{\partial t} = D_1 \nabla^2 \rho_1 - k_{-1} \rho_1 + \sum_{j=1}^{N_T} \sigma_1 \delta(\mathbf{r} - \mathbf{r}_j^T), \tag{8}$$

$$\frac{\partial \rho_2}{\partial t} = D_2 \nabla^2 \rho_2 - k_{-2} \rho_2 + \sum_{k=1}^{N_A} \sigma_2(\rho_1) \delta(\mathbf{r} - \mathbf{r}_k^A), \tag{9}$$

$$\frac{\partial \rho_3}{\partial t} = D_3 \nabla^2 \rho_3 - k_{-3} \rho_3 + \sum_{k=1}^{N_A} \sigma_3(\rho_1) \delta(\mathbf{r} - \mathbf{r}_k^A). \tag{10}$$

In Eqs (8)–(10), $\rho_i (i = 1, 2, 3)$ are functions of both time ($t \geq 0$) and space (on and around the multifunctional scaffold), each point is represented by a position vector, $\mathbf{r} = x\mathbf{i} + y\mathbf{j} + z\mathbf{k}$, where $x, y,$ and z are the coordinates and $\mathbf{i}, \mathbf{j},$ and \mathbf{k} are their corresponding unit vectors in the Cartesian coordinate system. $\nabla^2 = \partial^2/\partial x^2 + \partial^2/\partial y^2 + \partial^2/\partial z^2$ is the Laplace operator. D_i and k_{-i} are the diffusion and attenuation coefficients of ρ_i , respectively. Σ denotes the summation of all point-source terms. $\delta(\cdot)$ is the Dirac delta function, defined as $\delta(0) = 1$ and $\delta(\text{else}) = 0$. N_A is the total number of severed axons before their repair. N_T is the total number of CRMs-1 point sources, which depends on the density of HA/LV-NT-3 and HA/LV-BDNF seeded in the off-ramp area (Fig 1B; yellow) and on the chemical coarse-graining model. \mathbf{r}_j^T (immobile) is the position of the j -th point source of CRMs-1 (where $j = 1, 2, \dots, N_T$), and \mathbf{r}_k^A is the time-dependent position of the k -th growth cone capped on the regenerating axons ($k = 1, 2, \dots, N_A$). $\sigma_1, \sigma_2(\rho_1),$ and

$\sigma_3(\rho_1)$ are the point-source release rates of CRMs-1, CRMs-2, and CRMs-3, respectively. Note that $\sigma_2(\rho_1)$ and $\sigma_3(\rho_1)$ are the functions of ρ_1 , which indicates crosstalk or interactions between CRMs-1, CRMs-2, or CRMs-3. We can reduce the functions to $\sigma_2 = \sigma_{20}(1-R_L)$ and $\sigma_3 = \sigma_{30}R_L$ with $R_L = \rho_1/(K_d+\rho_1)$, where σ_{20} and σ_{30} are the normal release rates of CRMs-2 and CRMs-3 point sources, respectively, and K_d is the dissociation constant [32,38]. R_L defines receptor-ligand associativity on the growth cone membrane. $\sigma_{20}(1-R_L)$ and $\sigma_{30}R_L$ reflect the competitive relationship between CRMs-2 and CRMs-3. Eqs (8)–(10) are multi-component dynamic reaction-diffusion equations with nonlinear coupling of the point sources.

Numerical methods

Eqs (1)–(10) comprise the mathematical model of regenerative axons growing along the spherical multifunctional scaffold where their status is as shown in Fig 1A or Fig 2A–2C. The source terms in Eqs (9) and (10) are nonlinearly coupled with Eq (8) and Eqs (4)–(7) through point \mathbf{r}_k^A that tracks the growth cone. Therefore, Eqs (4)–(10) comprise a set of coupled nonlinear differential equations that can only be solved numerically.

The model is solved using three methods in three steps. The first step solves Eqs (8)–(10) for ρ_1 , ρ_2 , and ρ_3 using the lattice Boltzmann method (LBM) [47,48,49,50]. Using a central difference and interpolation scheme, the second step solves the gradients of ρ_1 , ρ_2 , and ρ_3 at the growth cone, and the axonal growth rates, using Eqs (6) and (7) and Eqs (2) and (3). Finally, the axonal growth path is obtained by integrating Eqs (6) and (7) and Eqs (2) and (3) using Euler’s method.

In the numerical simulation, we changed the lateral size of the scaffold (i.e., we changed the slope of the on-ramp/off-ramp) and the seeding densities of the HA/ECM components HA/LV-ChABC, HA/LV-NT-3, and HA/LV-BDNF. The simulation recorded the growth rates of the regenerating axons, and tested whether the regenerating axons could grow across the scaffold and finally connect with their targets.

Consideration of the parameter values

Based on data from in vitro experiments [35,36,37], we can estimate the order of magnitude of each parameter. The estimates are as follows: growth cone width $|\Delta \mathbf{r}_k^A|$ is approximately 10–20 μm ; axonal growth rate is approximately 0.01 $\mu\text{m s}^{-1}$; and the diffusion coefficient D_1 and dissociation constant K_d of CRMs-1 (e.g. NGFs) are approximately 10–50 $\mu\text{m}^2 \text{s}^{-1}$ and 1 nM, respectively. In addition, the range of concentrations for NGFs is $\sim(0.01-10)K_d$, and the minimum relative concentration difference to which the growth cone can respond [35,36,37,38,39], $|\Delta \rho_i/\rho_i|$, is $\sim 1\%$. However, the values of many parameters cannot be recognized, including the point-source release rate σ_i , the attenuation coefficients k_{-i} , the force proportionality constant λ_i , and the viscosity coefficient μ . Given that the diffusion velocity $k_{-1}\sqrt{D_1/k_{-1}}$ of CRMs-1 should exceed the constant velocity of the growth cone, the absolute concentration should satisfy $\rho_1 \geq K_d$ and the relative concentration difference should satisfy $|\Delta \rho_1/\rho_1| = |\Delta \mathbf{r}_k^A|/\sqrt{D_1/k_{-1}} \geq 1\%$ at the diffusion radius $\sqrt{D_1/k_{-1}}$. Under these conditions, the attenuation coefficient was estimated as $k_{-1} \geq 2.0 \times 10^{-6}$. At the point source, we should have $\rho_1 = eK_d + \sigma_1/k_{-1} \leq 10 K_d$ so that we can estimate the point-source release rate as $\sigma_1 = 1.82 \times 10^{-5} - 3.64 \times 10^{-4} \text{ nMs}^{-1}$. From $\rho_1 = K_d \exp(1 - r_{\text{max}}/\sqrt{D_1/k_{-1}}) \geq 0.01K_d$, the most effective diffusion radius was then estimated as $r_{\text{max}} = 5.6 \sqrt{D_1/k_{-1}}$. Finally, in the concentration field based on the above data, the axonal growth rate was assumed to be 0.0025–0.05 $\mu\text{m s}^{-1}$. After many numerical trials, the number of λ_i/μ was approximated as 1. The parameter values of CRMs-2 and CRMs-3 were set based on those of CRMs-1. All parameter values are listed in Table 1.

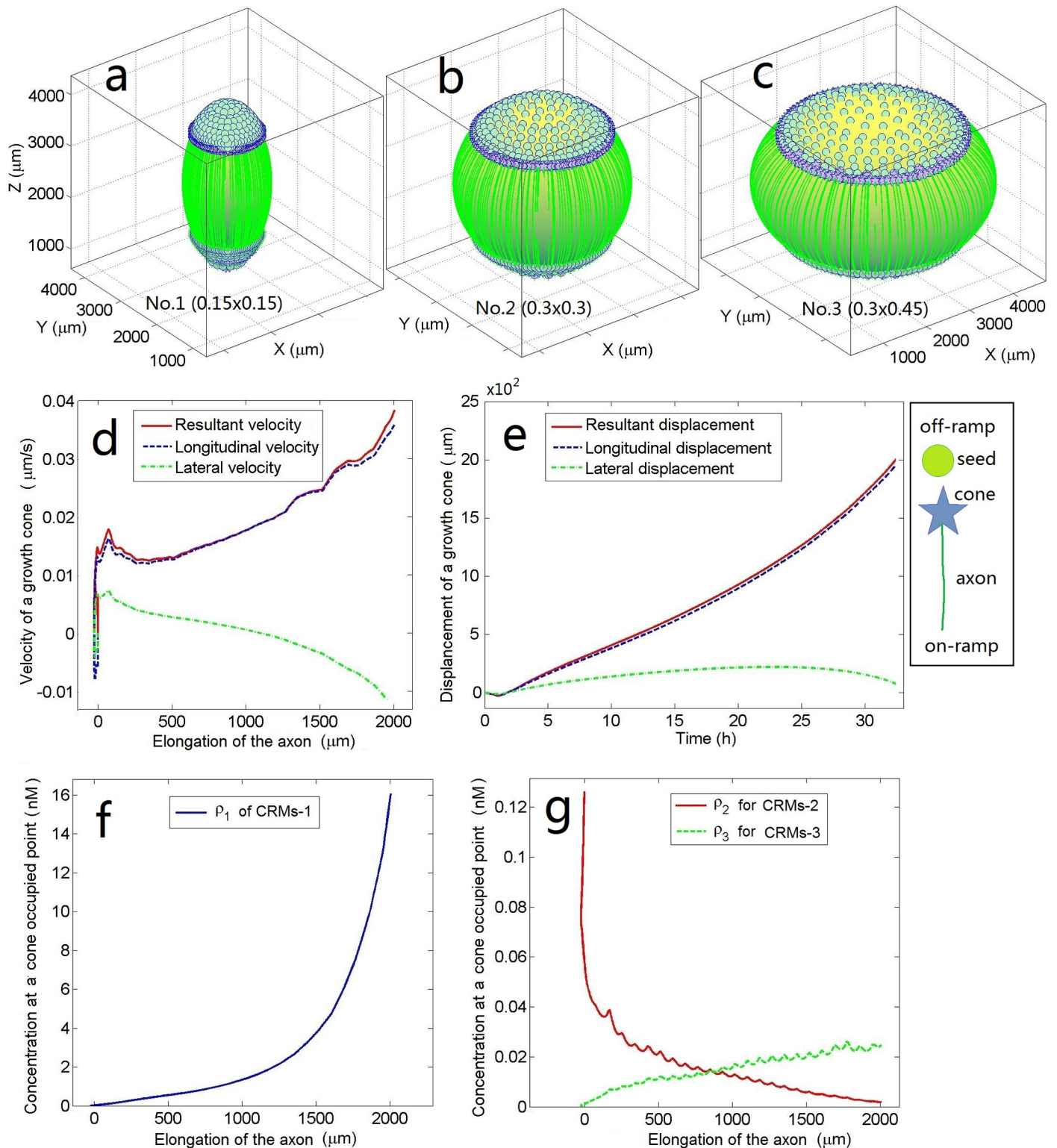


Fig 2. Three test scaffolds of different lateral sizes and some products. a)–c) The scaffolds and attached regenerated axons are separated and extracted from the models after calculation. In scaffolds No. 1, No. 2, and No. 3, the lateral semi-axis is $r_a = 0.15, 0.3,$ and 0.45 (or $0.75, 1.50,$ and 2.25 mm), respectively. The longitudinal semi-axis is $r_b = 0.3$ (or 1.5 mm) in all cases, and the number of severed axons is $N_A = 300$ in each calculation. The green bubbles with number $N_T = 300$ and density $\gamma_1 = 0.1 \mu\text{m}^{-2}$ embedded in the upper part (or the caudal/off-ramp) of each scaffold represent the coarsening point sources (or target cells) for CRMs-1 (two other seed types with densities $\gamma_2 = \gamma_3 = 0.1 \mu\text{m}^{-2}$ also cover the whole surface of each scaffold but are not shown). The green longitudinal lines (slightly fascicled) stemming

from the lower part (the rostral/on-ramp) of each scaffold represent the regenerated axons (numbering $0.78 N_A$, $0.7 N_A$, and $0.58 N_A$ in **a**, **b**, and **c**, respectively, corresponding to axonal regeneration success rates of 0.78, 0.7, and 0.58, respectively). **d**–**g**) Results related to a typical regenerating axon taken from the calculation of scaffold No. 1 (qualitatively similar results are obtained for the other two scaffolds). At the beginning, when the axon is at the on-ramp, its growth is unstable and some retraction is observed (**d** and **e**) because the concentrations of the positive factors CRMs-1 (f) and CRMs-3 are low (**g**; green), while those of the inhibitory factors are high (**g**; red). This situation is reversed as the axon approached the off-ramp.

<https://doi.org/10.1371/journal.pone.0205961.g002>

Equivalent number of seeds on the scaffold and the point-source release rate

To save computational resources, we employed coarse-grained processing, i.e., making up an equivalent number of seeds (point sources) for calculation that was smaller than that of seeding on the scaffold during fabrication. Because the fabrication process controls the densities of HA/ECMs/LV-ChABC, HA/LV-NT-3, and HA/LV-BDNF seeded on the scaffold, the densities of the point sources of CRMs-1, CRMs-2, and CRMs-3 can be quantified as $\gamma_1 = \eta_1 \gamma_1^0$, $\gamma_2 = \eta_2 \gamma_2^0$, and $\gamma_3 = \eta_3 \gamma_3^0$, respectively, where γ_1^0 , γ_2^0 , and γ_3^0 are the normal point-source densities of CRMs-1, CRMs-2, and CRMs-3 (in μms^{-2}) respectively, and η_1 , η_2 , and η_3 are their respective controllable scale factors. The areas of the scaffold off-ramp (caudal side) and the ventral portion of a growth cone are denoted by A_C and A_{cone} , respectively. Thus, the total number of CRMs-1 point sources in the off-ramp area is $\gamma_1 A_C$, i.e., $N_T = \gamma_1 A_C$ in Eq (8). Meanwhile, the total numbers of CRMs-2 and CRMs-3 connected to a single growth cone are $\gamma_2 A_{\text{cone}}$ and $\gamma_3 A_{\text{cone}}$, respectively. In Eqs (9) and (10), N_A is the total number of axons severed in an injury event. In a complete transection rat model, N_A might exceed 10^4 (estimated from the cross-sectional area ratio of an axon to the spinal cord). Because the exact value N_A was unavailable, we ranged N_A from 300 to 12000 in the simulations. Correspondingly, N_T and σ_1 in Eq (8) were replaced by their equivalent values N_{eqT} and σ_{eq1} , respectively. Considering $N_{\text{eqT}} = N_A$ and applying the mass conservation principle, we obtained $\sigma_{\text{eq1}} = \gamma_1 A_C \sigma_1 / N_A$, where $A_C / N_A = A_C / N_{\text{eqT}}$ represents the area occupied by each equivalent point source. Here, the point sources were assumed to be evenly distributed on the off-ramp of the scaffold. Similarly, σ_2 and σ_3 in Eqs (9) and (10) were replaced by their equivalent values $\sigma_{\text{eq2}} = \gamma_2 A_{\text{cone}} \sigma_2$ and $\sigma_{\text{eq3}} = \gamma_3 A_{\text{cone}} \sigma_3$, respectively, where A_{cone} represents the area on the scaffold surface covered by one moving growth cone at that moment and $\gamma_2 A_{\text{cone}}$ and $\gamma_3 A_{\text{cone}}$ represent the original numbers of CRMs-2 and CRMs-3 point sources on one A_{cone} , respectively. After an equivalent transformation, each A_{cone} includes two point sources: a CRMs-2 point source with release rate σ_{eq2} and a CRMs-3 point source with release rate σ_{eq3} . Both releases activate at the location of the cone and deactivate when the cone departs. This activation-deactivation process of the point sources is modeled by the Dirac delta function $\delta(\cdot)$ in Eqs (8)–(10).

In the simulations, we confined the architecture and mathematics of the model to a cubical compartment with side length $L = 5000 \mu\text{m}$ and imposed absolute boundary conditions. The D3Q15 mode [32,47] with a $64 \times 64 \times 64$ lattice was applied to LBM simulations. MATLAB 7.11.0 (The MathWorks, Inc.) was employed to program the simulations and run them on ThinkServer TD350 (Lenovo Group Ltd). All parameters used in the simulations are summarized in Table 1.

Results

Before describing the simulation results, we provide the following definitions. A severed axon is considered to have successfully regenerated when it has regrown along the scaffold surface from the on-ramp to the off-ramp within 2 weeks of treatment. The success rate of axonal regeneration is the number ratio of successfully regenerated axons to all severed axons in the injury event (calculated by the current mathematical model). The growth rate of the

Table 1. Parameters used in simulations.

Symbols	Definitions	Values	From
A_{cone}	ventral area of a growth cone	$100 \mu\text{m}^2$	[36,37,38,39]
A_C	area of the caudal region of the scaffold	related to scaffold size	Fig 1
D_1	diffusion coefficient of CRMs-1	$50 \mu\text{m}^2\text{s}^{-1}$	[38], Eq (8)
D_2	diffusion coefficient of CRMs-2	$10 \mu\text{m}^2\text{s}^{-1}$	Eq (9)
D_3	diffusion coefficient of CRMs-3	$10 \mu\text{m}^2\text{s}^{-1}$	Eq (10)
k_{-1}	attenuation coefficient of CRMs-1	$1.25 \times 10^{-3}\text{s}^{-1}$	Eq (8)
k_{-2}	attenuation coefficient of CRMs-2	$2.5 \times 10^{-3}\text{s}^{-1}$	Eq (9)
k_{-3}	attenuation coefficient of CRMs-3	$2.5 \times 10^{-3}\text{s}^{-1}$	Eq (10)
K_d	dissociation constant of CRMs-1/2/3	1 nM	[38], Eqs (9) and (10)
L	side length of the computation domain	5000 μm	Fig 1
N_A	total/equivalent number of severed axons	300–12000	Eqs (9) and (10)
N_T	total/equivalent number of target cells	300–12000	Eq (8)
r_a	semi-axes of ellipsoid/scaffold	0.15–0.45, scaled by L	Fig 1B
r_b	semi-axes of ellipsoid/scaffold	0.3, scaled by L	Fig 1B
r_C	maximum rotational radius of scaffold caudal	$0.75r_a$	Fig 1B
r_R	maximum rotational radius of scaffold rostral	$0.75r_a$	Fig 1B
$ \Delta r_k^A $	width of a growth cone	10 μm	[38], Eq (5)
γ_1^0	normal density of the point source of CRMs-1	$0.1 \mu\text{m}^{-2}$	Eq (8)
γ_2^0	normal density of the point source of CRMs-2	$0.1 \mu\text{m}^{-2}$	Eq (9)
γ_3^0	normal density of the point source of CRMs-3	$0.1 \mu\text{m}^{-2}$	Eq (10)
λ_1	force proportionality constant of CRMs-1	$1 \text{ nN } \mu\text{m}^{-1}$	Eq (5)
λ_2	force proportionality constant of CRMs-2	$1 \text{ nN } \mu\text{m}^{-1}$	Eq (5)
λ_3	force proportionality constant of CRMs-3	$1 \text{ nN } \mu\text{m}^{-1}$	Eq (5)
μ	dynamic viscosity coefficient	$1 \text{ nN } \mu\text{m}^{-2}\text{s}$	Eq (4)
σ_1	normal release rate of a CRMs-1 point source	$6.75 \times 10^{-5} \text{ nMs}^{-1}$	Eq (8)
σ_{20}	normal release rate of a CRMs-2 point source	$6.75 \times 10^{-5} \text{ nMs}^{-1}$	Eq (9)
σ_{30}	normal release rate of a CRMs-3 point source	$6.75 \times 10^{-5} \text{ nMs}^{-1}$	Eq (10)
$\sigma_{\text{eq}1}$	equivalent σ_1	$\gamma_1 A_C \sigma_1 / N_A$	Eq (8)
$\sigma_{\text{eq}2}$	equivalent σ_2	$\gamma_2 A_{\text{cone}} \sigma_2$	Eq (9)
$\sigma_{\text{eq}3}$	equivalent σ_3	$\gamma_3 A_{\text{cone}} \sigma_3$	Eq (10)
η_1	density scale factor for CRMs-1	$\eta_1 = \gamma_1 / \gamma_1^0$, controllable	Eq (8)
η_2	density scale factor for CRMs-2	$\eta_2 = \gamma_2 / \gamma_2^0$, controllable	Eq (9)
η_3	density scale factor for CRMs-3	$\eta_3 = \gamma_3 / \gamma_3^0$, controllable	Eq (10)

<https://doi.org/10.1371/journal.pone.0205961.t001>

regenerated axons is the average longitudinal extension velocity of all successfully regenerated axons (calculated as $(\sum_{k=1}^{N'_A} V_{zk}) / N'_A$, where V_{zk} is defined in Eq (6), and $N'_A = N_A \times$ success rate). The growth rate should exceed $0.0025 \mu\text{ms}^{-1}$ (1.5 mm per week) but should not exceed the physiological limit ($\sim 0.05 \mu\text{ms}^{-1}$). The effective growth rate of the axons is the product of their success and growth rates, i.e., the longitudinal extension velocity averaged over all severed axons in the injury and repair process. It is given by $(\sum_{k=1}^{N_A} V_{zk}) / N_A$.

Influence of the number of severed axons on regeneration

The number of severed axons N_A usually depends on the damage event. As previously mentioned, the maximum number of severed axons might be in the order of 10^{-4} . In the following computer simulations, we varied N_A from 300 to 12000 and observed the consequent changes

in the growth and success rates of post-SCI axonal regeneration. Next, we considered three scaffolds (No. 1, No. 2, and No. 3, sized at $r_a \times r_b = 0.15 \times 0.3$, 0.3×0.3 , and 0.45×0.3 , respectively) and determined the most efficient size for axonal regeneration. For this purpose, we investigated how the slope of the on-ramp/off-ramp of the scaffold affects axonal regeneration. In this section, the density scale factors of the CRMs-1, CRMs-2, and CRMs-3 point sources on the scaffolds were considered as $\eta_1 = \eta_2 = \eta_3 = 1$. In other words, the seed densities were constant and set to the same value (specifically, $\gamma_1 = \gamma_2 = \gamma_3 = 0.1 \mu\text{m}^{-2}$; see Table 1 and the subsection “Equivalent number of seeds on the scaffold and the point-source release rate” for details). All other parameter values are listed in Table 1. To clarify the scope and level of the model and the developed method, we first discuss the special case of $N_A = 300$. Fig 2 demonstrates the growth path and velocity of the regenerative axons and the CRM concentrations around the growth cone. By increasing N_A from 300 to 12000 at irregular intervals, we obtained a series of results similar to those demonstrated in Fig 2. These results are shown in Fig 3, which reveals how the number of severed axons influences axonal regeneration.

Fig 3A shows the effect of the number of severed axons N_A on the growth rate of the regenerating axons on each scaffold. Each point in the curves indicates the average growth rate of the surviving axons that grew along the scaffold from the on-ramp to the off-ramp. Axons that died or failed halfway were excluded. The error bars indicate the standard deviations of the averages. N_A does not significantly affect the growth rate provided that the axons can successfully regenerate. Moreover, the growth rate is proportional to the lateral size of the scaffold.

In Fig 3B, the success rate of axonal regeneration decreases with increasing N_A . When N_A was moderately large (< 9000), the slim scaffold achieved a high success rate. When $N_A = 300$, the success rate was approximately 35% higher on scaffold No. 1 than on scaffold No. 3; however, when $N_A = 12000$, the lateral size effect of the scaffold disappeared and the success rates on all three scaffolds declined to $< 30\%$. As the number of severed axons increased from 300 to 12000 on scaffold No. 1, the success rate was reduced by a factor of 3. From Fig 3A and 3B, we infer that a small on-ramp slope (i.e., a slim scaffold) increases the success rate of axonal regeneration up to a certain number of severed axons. When too many regenerative axons pass over the narrow bridge, the congestion lowers the growth rate. If success rate is more important than growth rate, the slim scaffold would be the first choice.

Fig 3C shows the effective growth rate of the axons (the product of the growth rate in Fig 3A and the success rate in Fig 3B as N_A increases). Each point in the curves represents the growth rate of all regenerated axons, averaged over all severed axons, in the injury and repair process. The effective growth rate is a comprehensive index of axial sprouting and growth of axons after an SCI. Again, the slim scaffold is advantageous for axonal regeneration when $N_A \leq 6000$.

In Fig 3D, the concentration of CRMs-1 sensed by the regenerating axons was relatively robust to both N_A and the lateral size r_a of the scaffold. However, the concentration ratio of CRMs-3 to CRMs-2 sensed by the regenerating axons heavily depended on both N_A and r_a (Fig 3E). Note that N_A and r_a are also highly correlated with the success rate of axonal regeneration (Fig 3B) and the effective axonal growth rate (Fig 3C). This suggests that the concentration ratio of CRMs-3 to CRMs-2 deserves more attention than it currently receives in SCI treatments.

Fig 3F averages the longitudinal coordinates in Fig 3B over the number of horizontal coordinates on scaffolds No. 1, No. 2, and No. 3. Again, the slim scaffold is beneficial for SCI treatments. In other words, irrespective of the number of severed axons, the slim scaffold is always the first choice for bridging. Therefore, the next two sections are devoted to scaffold No. 1 (slim scaffold with size 0.15×0.3).

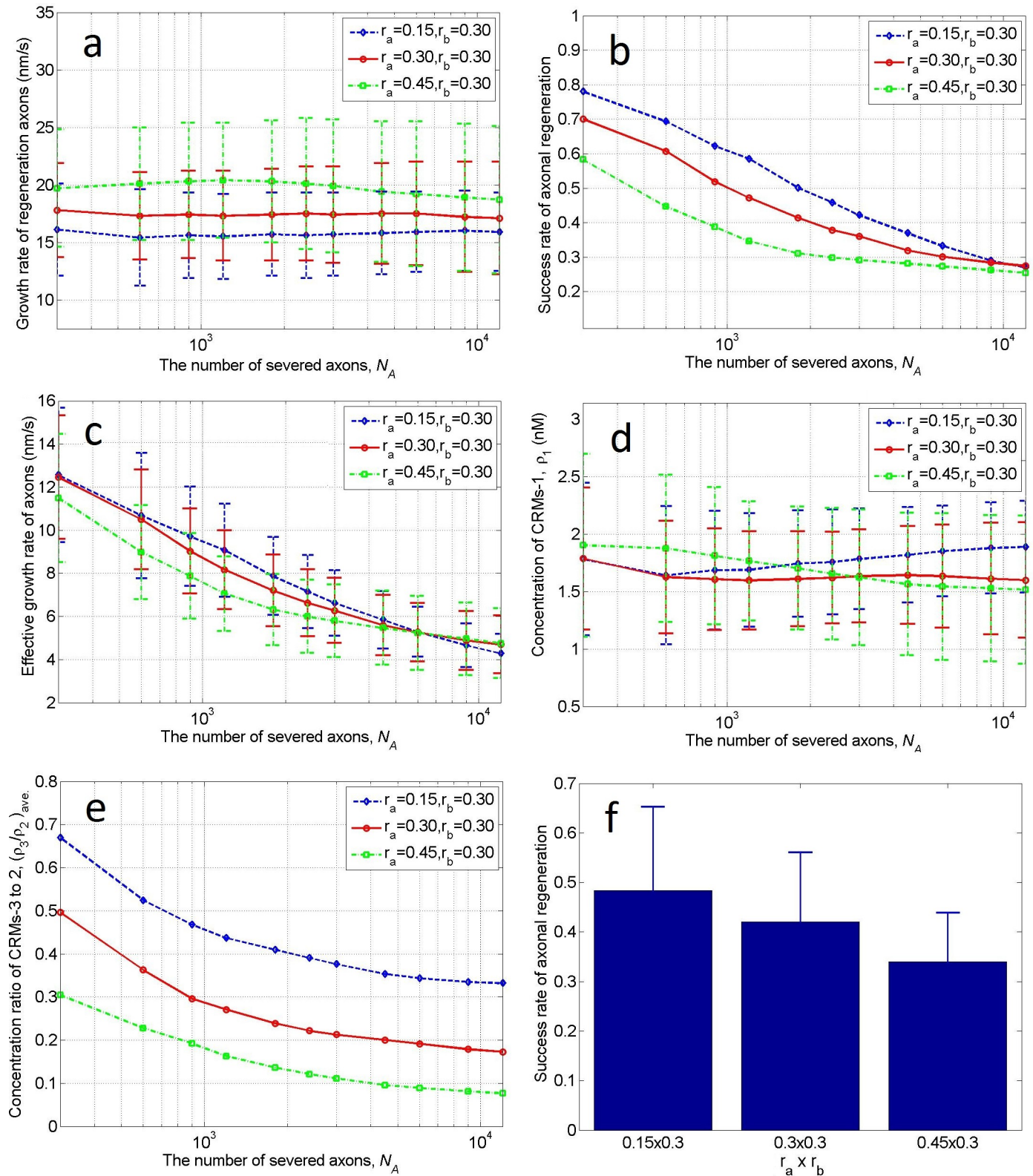


Fig 3. Influence of the number of severed axons on axonal regeneration. a) Growth rate of regenerating axons, b) success rate of axonal regeneration, c) effective growth rate, d) concentration of CRMs-1, and e) concentration ratio of CRMs-3 to CRMs-2, plotted as functions of $\log_{10} N_A$, where N_A is the number of severed axons. The curves in each panel were obtained on scaffold No. 1 (0.15×0.3), No. 2 (0.3×0.3), and No. 3 (0.45×0.3), respectively. f) Longitudinal coordinates in panel b averaged over the number of horizontal coordinates on scaffolds No. 1, No. 2, and No. 3 (left to right). Error bars indicate the standard deviations.

<https://doi.org/10.1371/journal.pone.0205961.g003>

Influence of CRMs-1 point-source density on regeneration

This analysis was performed on scaffold No. 1 ($r_a \times r_b = 0.15 \times 0.3$). The prototype of the CRMs-1 point source is HA/LV-NT-3 and HA/LV-BDNF seeded on the off-ramp (Fig 1B, yellow) of the scaffold during fabrication (see subsection “Coating and seeds for the scaffold”). In each test, the seeding density of CRMs-1 was $\gamma_1 = \eta_1 \gamma_1^0$ ($\gamma_1^0 = 0.1 \mu\text{m}^{-2}$; see Table 1), where η_1 was increased from 0 to 100 at irregular intervals. Alternatively, the CRMs-2 point source includes various inhibitory components, for example MAG induced by debris from the myelin sheath resulting from when axons were damaged, and CSPGs remaining on the scaffold surface, which cannot be easily controlled. Here, the density of the CRMs-2 point source was graduated through six levels: $\gamma_2 = \eta_2 \gamma_2^0$ ($\gamma_2^0 = \gamma_1^0 = 0.1 \mu\text{m}^{-2}$, with $\eta_2 = 0, 1, 5, 10, 50, \text{ and } 100$). The density of the CRMs-3 point source was then expressed as $\gamma_3 = \eta_3 \gamma_3^0$. CRMs-3 represents the HA/ECM components (collagen I, fibronectin, and laminin I) coated on the whole surface of the scaffold during fabrication. Therefore, we set $\eta_3 = 1$ (or $\gamma_3 = \gamma_3^0 = 0.1 \mu\text{m}^{-2}$, a constant). The number of severed axons can be selected from the feasible range (300–12000). Considering the available computer resources, we maintained N_A to be constant at 1200. Under these conditions, we performed the calculation and obtained Fig 4.

Fig 4A shows the growth rates of the regenerating axons as functions of density (η_1) of the CRMs-1 point source for different densities (η_2) of the CRMs-2 point source. Axonal growth is driven by the concentration gradient of CRMs-1 ($\nabla \rho_1$) and is supported and inhibited by $\nabla \rho_3$ and $\nabla \rho_2$, respectively. Note that ρ_2 and ρ_3 are coupled to ρ_1 through Eqs (8)–(10). Therefore, the growth rates of the regenerating axons are not simply proportional to η_1 but change nonlinearly with increasing η_1 . Moreover, their extreme values depend on η_2 . Note that the growth rate was always lowest when $\eta_2 = 0$, i.e., when no inhibitors were present in the injured microenvironment. This suggests that some remaining inhibitors (e.g., $0 < \eta_2 \leq 1$) are required to increase the growth rate. However, when $\eta_1 > 15$ and $\eta_2 > 5$, the growth rates were quite similar, suggesting that once the inhibitor level has exceeded a certain threshold, simply increasing the promoter levels is ineffective for increasing the growth rate.

Fig 4B shows the success rate of axon regeneration with increasing density (η_1) of the CRMs-1 point source. First, when $\eta_2 = 0$, i.e., when no inhibitor was present in the injured microenvironment, the success rate was 100% for all η_1 , except when $\eta_1 = 0$ (i.e., when the success rate was 0). Next, for any fixed $\eta_1 > 0$, increasing η_2 decreased the success rate. Finally, when η_1 was sufficiently high, the success rate of axonal regeneration exceeded 92%, regardless of η_2 . This suggests that reducing the inhibitor while increasing the promoter improves the success rate of axonal regeneration. The latter may be more important than the former because even if η_2 reached 0, $\eta_1 > 0$ would be required for axonal growth. However, as previously mentioned, a high success rate implies overcrowding of the growing axons on the scaffold, which eventually causes congestion and lowers the axonal growth rate. If the growth rate is excessively low, the axons might abort the growth process (in practice, growth cessation is due to unexpected causes) or an opportunistic time window for subsequent treatments may be missed. Therefore, when predicting axonal regeneration, the success rate must be balanced against the growth rate of the regenerating axons.

Fig 4C shows the effective growth rate of the axons. As previously mentioned, this index represents the sprouting and growth of the injured axons. Additionally, it is the product of the growth rates in Fig 4A and the success rates in Fig 4B. The effective growth rates were higher for $\eta_1 > 5$ and $\eta_2 = 1$ than for $\eta_2 = 0$. If $\eta_1 > 50$ could be achieved in practice, three treatments ($\eta_1 > 5$ and $\eta_2 = 1$, $\eta_1 > 30$ and $\eta_2 = 5$, and $\eta_1 > 50$ and $\eta_2 = 10$) are preferred over the $\eta_2 = 0$ treatment, and increasing η_1 is much easier than achieving $\eta_2 = 0$.

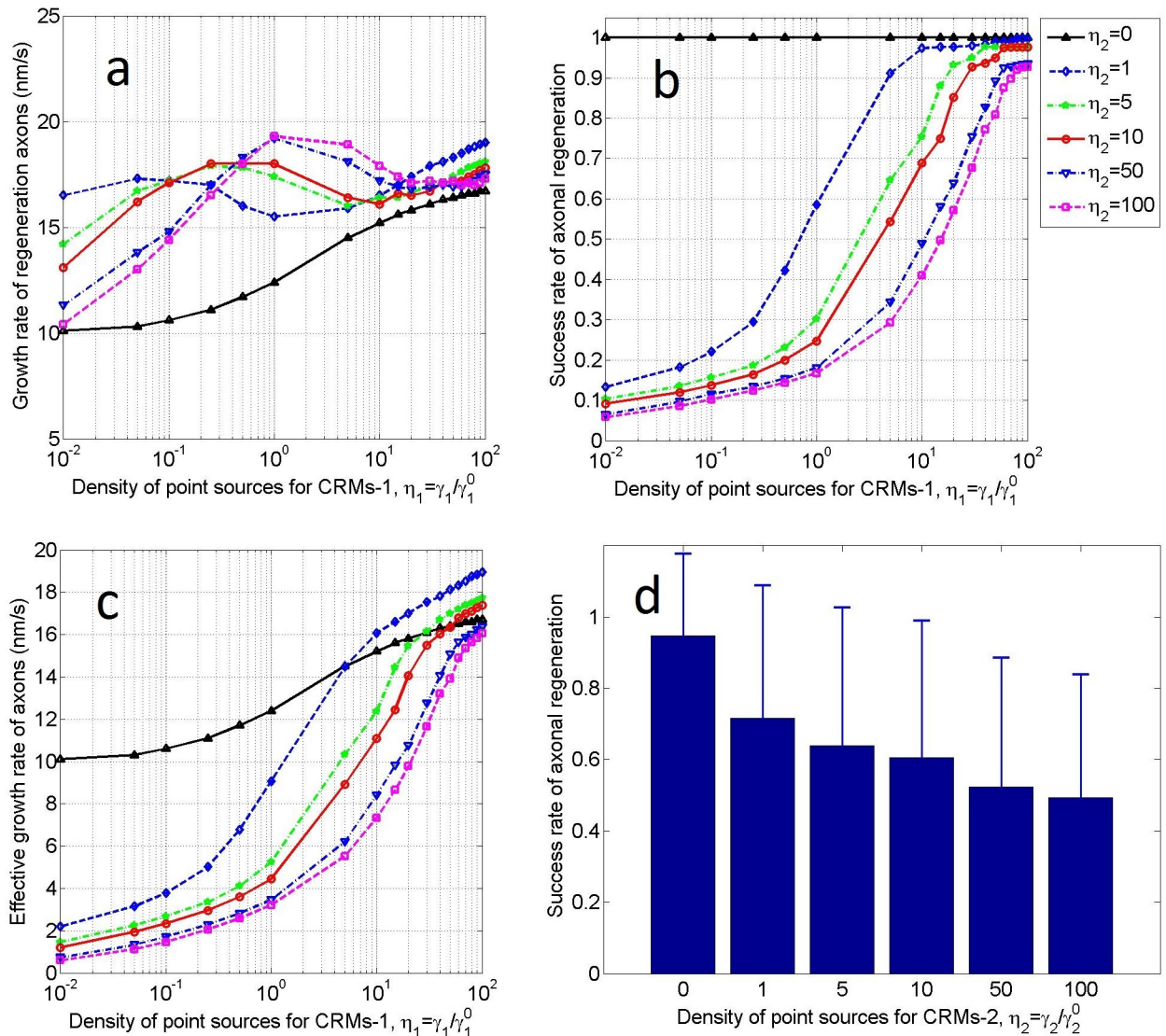


Fig 4. Influence of CRM1-1 point-source density on axonal regeneration. a) Growth rate of regenerated axons, b) success rate of axonal regeneration, and c) effective growth rate of axons as functions of the density (η_1) of the CRMs-1 point source. Results are plotted for different densities (η_2) of the CRMs-2 point source. The test scaffold is sized as $r_a \times r_b = 0.15 \times 0.3$, the CRMs-3 point source density is $\eta_3 = 1$, and the number of severed axons is $N_A = 1200$. d) Success rate of axonal regeneration averaged over $\eta_1 = 0-100$ for each η_2 .

<https://doi.org/10.1371/journal.pone.0205961.g004>

Fig 4D shows the average success rates of axonal regeneration over all η_1 (0–100) for each η_2 . Regardless of η_1 , the success rates on scaffold No. 1 decreased with increasing η_2 and the marginal effect was large for small η_2 . Again, this result highlights that reducing the inhibitors in the microenvironment is important for axonal regeneration. Note that when $\eta_2 = 0$, the average success rate should be less than one (below 100%) because the success rate at $\eta_1 = 0$ was zero. Thus, its logarithm (horizontal axis in Fig 4B) could not be defined. However, owing to non-zero η_1 a unity success rate was achieved (Fig 4B).

Influence of CRMs-3 on axonal regeneration

Finally, we numerically test the hypothesis that an over-eutrophic scaffold surface harms axonal regeneration.

The analysis was performed on scaffold No. 1 ($r_a \times r_b = 0.15 \times 0.3$), and assumed a constant number of severed axons ($N_A = 1200$). The prototype of the CRMs-3 point source comprises HA/ECM components (collagen I, fibronectin, and laminin I) coated on the whole surface of the scaffold, as described previously. The coating density of CRMs-3, expressed as $\gamma_3 = \eta_3 \gamma_3^0$ with $\gamma_3^0 = 0.1 \mu\text{m}^{-2}$ (see Table 1), can be set during fabrication. In each test, density η_3 was increased from 0 to 100 at irregular intervals. The CRMs-1 and CMRs-2 point-source densities were set as $\gamma_1 = \eta_1 \gamma_1^0$ (with $\gamma_1^0 = 0.1 \mu\text{m}^{-2}$ and $\eta_1 = 1$) and $\gamma_2 = \eta_2 \gamma_2^0$ (with $\gamma_2^0 = 0.1 \mu\text{m}^{-2}$ and $\eta_2 = 0, 1, 5, 10, 50, \text{ and } 100$), respectively. The calculation results under these conditions are presented in Fig 5.

As shown in Fig 5A, the growth rates of the regenerating axons decreased with increasing η_3 of the CRMs-3 point-source density, regardless of η_2 . Over a wide range of lower η_3 values, the growth rates remained stable for all η_2 , except for $\eta_2 = 0$. However, beyond a threshold η_3 value, which increased with increasing η_2 , growth sharply declined. This supports the hypothesis that an over-eutrophic scaffold surface impedes axonal growth, and that certain inhibitors might naturalize the over-eutrophic effect and weaken or delay the harm.

Fig 5B shows the success rates of axonal regeneration varying as functions of η_3 for each η_2 . When $\eta_2 = 0$, i.e., when no inhibitor was present in the injured microenvironment, the success rate remained at 100% till the point when $\eta_3 = 60$, and then dropped sharply to 16.67% at $\eta_3 = 70$. Subsequently, the success rate fell to zero. At non-zero η_2 , the success rates first slowly ascended with increasing η_3 , then rose sharply before dropping to a low level, and finally reached zero. When η_2 was high, the success rate curve began at a low level and ascended very slowly, forming a low plateau. For $\eta_2 \geq 50$, the success rate peaked only when η_3 exceeded 100. This suggests that the use of an over-eutrophic scaffold surface to improve the success rate of axonal regeneration is inefficient and risks destabilization of the regeneration process.

Fig 5C plots the effective growth rate of the axons as functions of η_3 for each η_2 . Applying an over-eutrophic scaffold surface to promote the sprouting and growth of axons after an SCI might be inefficient or even counterproductive.

Fig 5D shows the average success rates of axonal regeneration over $\eta_3 = 0-100$ for each η_2 . Regardless of η_3 , the success rates decreased with increasing η_2 on identical scaffolds and the marginal effect was greater at low η_2 than at high η_2 . As discussed earlier, this result highlights the fact that reducing inhibitors in the microenvironment is important for axonal regeneration.

Discussion

This study specifically aimed to create a microenvironment for axonal regrowth after SCI by mathematically changing the location of seeding on the scaffold, the density of the cells/factors seeded, and the size and shape of the scaffold. Therefore, we assumed a solid, spherical, multifunctional, biomaterial scaffold that bridges the rostral and caudal stumps of a completely transected spinal cord in a rat model for the calculations.

We assumed the body of the scaffold was made of PLG, the whole surface was coated with HA/ECMs and HA/LV-ChABC, and its off-ramp at the caudal area was additionally seeded with HA/LV-NT-3 and HA/LV-BDNF. These factors perform several functions. First, the on-ramp slope at the rostral area of the scaffold steers the growth cones of the regenerative axons onto the scaffold smoothly. Second, the factors seeded on the scaffold surface can be localized and sustained over a reasonably long period of time. The HA/ECM components adhere to the growth cones on the scaffold, supporting regenerative axons. HA/LV-ChABC secretes ChABC, which degrades CSPGs, inhibitory components from the glial scars surrounding the injured tissue. The NT-3 and BDNF molecules released from HA/LV-NT-3 and HA/

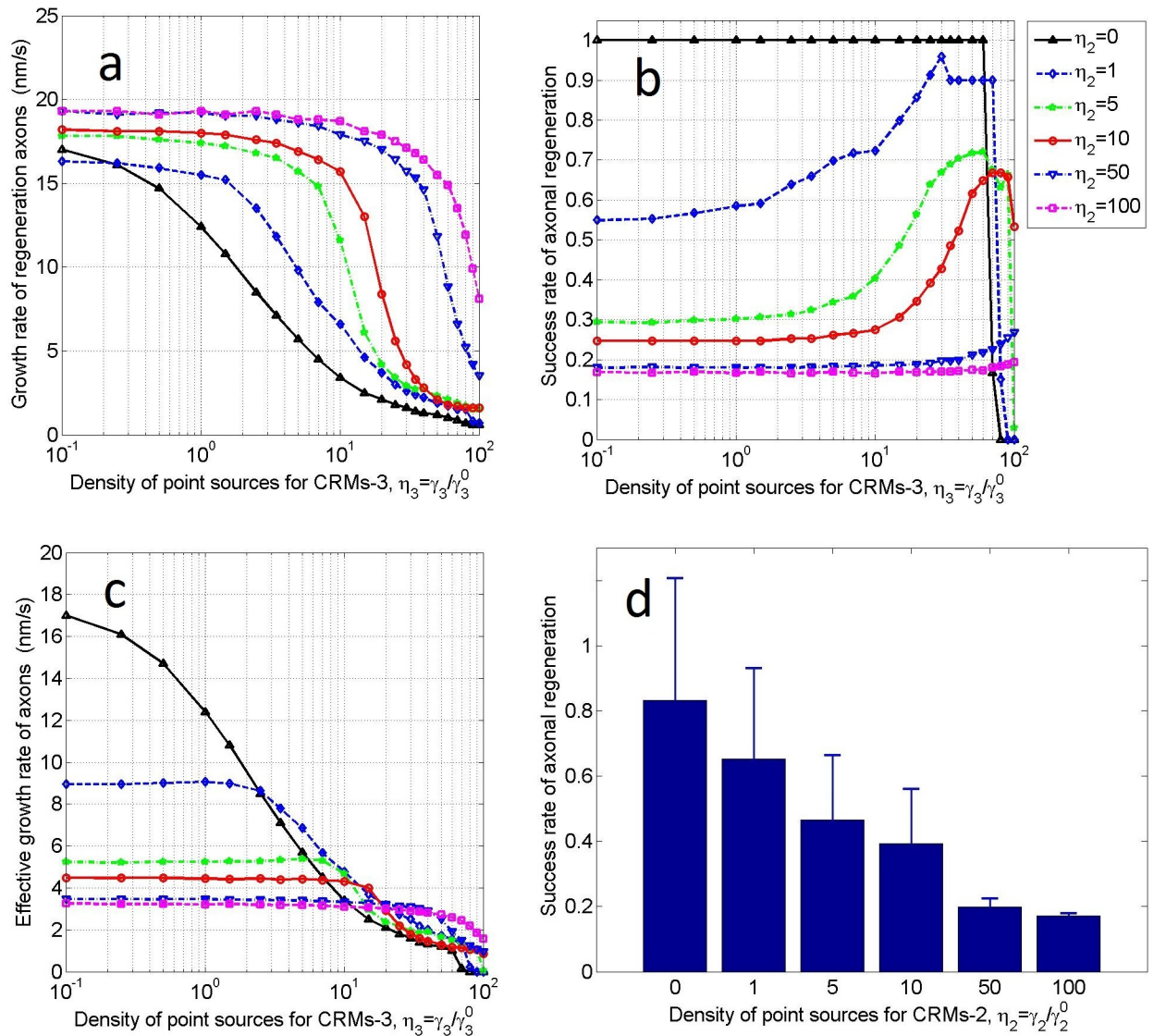


Fig 5. Influence of CRMs1-3 point-source density on axonal regeneration. a) Growth rate of regenerating axons, b) success rate of axonal regeneration, and c) effective growth rate of axons as functions of CRMs-3 point-source density for different densities (η_2) of the CRMs-2 point source. The test scaffold is sized as $r_a \times r_b = 0.15 \times 0.3$, the CRMs-1 point-source density is $\eta_1 = 1$, and the number of severed axons is $N_A = 1200$. d) Success rate of axonal regeneration averaged over $\eta_3 = 0-100$ for each η_2 .

<https://doi.org/10.1371/journal.pone.0205961.g005>

LV-BDNF at the off-ramp area can diffuse to the on-ramp area; this gradient can then guide the axons at the rostral stump to grow along the outer surface of the scaffold and enter the caudal stump area, while also preventing the axons regenerating at the caudal stump from growing toward the rostral stump until they connect with axons emerging from the on-ramp area. That is, the scaffold forms a one-way bridge from the rostral to the caudal side, with a gentle slope of entry. From a mathematical point of view, the profile curve of the scaffold results in a small and continuous tangent slope, and the resulting concentration of all factors (promoters and inhibitors) on and around the scaffold, and varying along the span of the scaffold from one side to another, causes a monotonic increase. Provided that the scaffold is implanted upside down, the gradient of the resulting concentration or the direction of growth of axons will be reversed correspondingly, inferring from previous observations [18] that axons grow toward a

site where additional cells have been injected, so either side of the bridge could be used as an injection site. Note that no matter which side of the bridge is used as the entry point, both motor and sensory neurons axons can cross the bridge because axons of both motor and sensory origins have previously been found within a tunneled scaffold [14].

Several scaffolds for SCI have previously been described [3,4,5,6,7], such as cell grafts [8,9], tubes or conduits [10], and cylinders with tunnels/linear pores or filled with fibers, either randomly or in alignment. Of these, cell grafts comprise natural soft tissues, with conduits that are empty or contain soft matrices and/or cells, and with a wide diameter, making it easy for regenerative axons to enter them, with no need to consider an entry slope. However, axons which entered these grafts were often trapped in them and rarely re-entered the host tissue. It was commonly believed that fine physical guidance was required within the cell grafts and conduits. Therefore, cylinders with tracks (a rolled-up nanofiber sheet or film) [10,11] or tunnels (via modeling) [14,19], combined with seeding of cells/factors [12,13,14,15,16,18,19], emerged and mostly replaced the use of cell grafts and conduits. However, not only did regenerative axons still get trapped in the guideways [10,11,12,13,14,15,16], but congestion was also observed at the entries [19]. This trapping, according to the current study, is caused by the over-eutrophication in and/or on the scaffold, and the lack of additional chemotactic factors close to either side of the scaffold. Even if these factors are uniformly distributed throughout whole scaffold during fabrication, because the factors diffuse easily from the two ends of the scaffold, they reach the middle of the scaffold after a period of time, which attracts regenerating axons from both ends to the middle. Therefore, the scaffold becomes a two-way channel, leading the axons to grow toward each other, probably resulting in their intersection. However, there is little direct evidence to show that such intersected axons can form synaptic connections. In this situation, the factors on the scaffold are more likely to be a barrier against the regenerating axons. Fortunately, the axons can sometimes break through this barrier [19], as was simulated in this study, and re-enter the host tissue. This is typically due to additional chemotactic factors being set close to either the caudal [19] or rostral stumps [18]. Alternatively, factors (known or unknown) contained in and/or on the scaffold might form (intentionally or unintentionally) a consistent gradient along the span of the bridge; there may also be a small probability that some unknown factors from host tissues form a beneficial gradient for axonal regeneration. Based on the typical situation [19], we inferred that, according to the principle of chemotaxis of axons, only if the peak of the barrier is much lower than the summit formed by the chemotactic factors at either end, the axons can break through the barrier.

However, another barrier that exists for scaffolds with tracks or tunnels is the entry obstruction that lowers the number of axons entering into the spaces or pores of the scaffold because of the absence of a uniform entry slope. For tunneled scaffolds [14, 19], the slope of entry is small or zero only for those axons whose growth cones face to the pores, where the axonal incidence angle $\alpha = 0$ (i.e., the slope = $\tan(0) = 0$); whereas for the other axons at the entry, the slope is abrupt or infinite, due to $\alpha = \pm\pi/2$ (i.e., slope = $\tan(\pm\pi/2) = \pm\infty$). This prevents the axons from regenerating straight ahead and reduces the number of axons entering the tunnels. Pore size is another parameter that affects the ability of axons to pass through a scaffold, and while investigating optimal pore size is difficult, the present model can be modified to study this. Once the number of axons entering a scaffold is small, the number of axons exiting will be much lower, according to previous observations [19]. The present spherical scaffold described by us is not only simple but also, at least theoretically, lacks the shortcomings inherent in other porous scaffolds.

The proposed scaffold could be used to replace previous scaffolds used in rat models for SCI repair [10,11,16], to bridge a gap of approximately 3 mm. It is worth noting that the present scaffold might offer additional possibilities. The complex seeded on the caudal area that

express NT-3 and BDNF, as well as being diffusible chemoattractants for attracting axonal growth cones, have enhanced oligodendrocyte survival and axon myelination [24,51,52,53]. NT-3 and BDNF may also enhance a number of other processes. For instance, BDNF has been associated with a reduction in the inflammatory response, including a reduction in astrocyte numbers [54], which further aids axon regeneration. While fabrication of our scaffold might be difficult, and the use of hydroxylapatite (HA) is probably not the best choice due to the risk of Milwaukee shoulder [34], we do provide a prospective direction for SCI repair.

Our mathematical model embodies the geometry, chemistry, and physics of the system under investigation. The shape and size of the scaffold provide the geometrical boundary conditions that constrain the growth cone's movement or the regenerative axon growth. While the inclusion of all chemical factors in a single model is difficult, a coarse-grained method can be used to obtain a balance between the reduction in the number of factors and the retention of the chemical properties. That is, the CRMs on and around the scaffold (assuming it has been implanted) were classified into three types with different chemical properties: the CRMs-1 group comprised chemoattractants of axonal growth (NT-3/BDNF secreted by seeded HA/LV-NT-3 and HA/LV-BDNF at the off-ramp area); the CRMs-2 group comprised chemorepellents of axonal growth (compounds produced by the injured tissue, such as Nogo-60, MAG, and OMG, and the remnant CSPGs that are not neutralized by ChABC released from seeded HA/LV-ChABC); and the CRMs-3 group comprised molecules released from the coated HA/ECM components, which support axonal growth. Among these groups, CRMs-1 plays the leading role in axonal regeneration, whereas CRMs-2 and CRMs-3 provide a balanced and coordinated effect, and interact with CRMs-1 (for which, CRMs-2/3 was formulated as a function of CRMs-1). The physical and biophysical aspects of the model are the Fickian diffusions and reactions of the CRMs and the chemotaxis of the axonal growth cone motility. Under CRMs-1 and CRMs-3 gradients, the regenerative axons elongate toward the target cells, whereas under the CRMs-2 gradient, they retract. A similar chemotaxis pattern has been validated via experiments [35,36,37], and mathematically modeled for studying axonal growth in neural development [28,29,30,31]. Note that axonal growth/regrowth follows the same processes observed experimentally both in development and injury, *in vivo* and *in vitro*, because in both cases the experiments always initially cause damage to the nerve cells, for instance during surgery or separation. The difference between them, however, is in the degree of damage, and in the age of the experimental subjects. Therefore, a theoretical model for axonal growth during development can be modified for studying SCI. In fact, the present model is mathematically similar to those described in the literature [28,29,30,31].

By applying our mathematical model to the theorized scaffold, we numerically studied the influence of the number of severed axons; the slope of the on-ramp of the scaffold (which is related to the lateral size of the scaffold); and the concentrations and gradients of the CRMs (which are related by their seeding densities to the survival and growth of the regenerative axons).

Axonal regeneration was evaluated based on the growth and success rates of the regenerated axons. A severed axon has successfully regenerated when it has regrown along the scaffold surface from the on-ramp to the off-ramp within 2 weeks of the treatment. The success rate defines the number ratio of the successfully regenerated axons to all axons severed in an injury event. The growth rate is the average longitudinal extension velocity of the successfully regenerated axons.

It should be noted, however, that our model is highly idealized, for example, the basis data we used for the calculation of growth cone velocity were not derived from trauma tissue, which might be spatially different in physics and chemistry, and not be reflected by CRMs-2. The intersections and/or tangles between regenerating axons and the energy expenditure for

axonal growth were not modeled in the current study. The cut to generate a spinal cord injury should not be too wide (>1 cm) for using this model to predict SCI because the effective diffusion distance of CRMs-1 might be limited to approximately 1 cm by Fick's first law, on which this model is based. Only an *in vivo* verification will show whether these equations will hold.

Conclusions

A solid, spherical, multifunctional, biomaterial scaffold is assumed to bridge the rostral and caudal stumps of the spinal cord in a completely transected rat model, thereby promoting the entry of regenerative axons from the rostral stump into the caudal stump tissue at the opposite side of the scaffold.

Three scaffold shapes (slim, round, and stocky) were investigated in our simulations. Among them, the slim shape benefited axonal regeneration the most by presenting a small slope at the on-ramp area. However, if the success rate becomes too high, numerous regenerative axons crowd into a narrow area, causing congestion and resulting in a reduced growth rate. The stocky scaffold induced the opposite effect, and the round scaffold induced intermediate effects. When success rate is more important than growth rate, the slim scaffold should be the first choice.

The number of severed axons in an injury event (between 300 and 12000) does not significantly affect the growth rate of the regenerated axons, but does influence the success rate of axonal regeneration (particularly, the success rate decreases with increasing number of severed axons).

Among the three types of chemical treatments, raising the CRMs-1 (NT-3 and BDNF) level while reducing the CRMs-2 level (CSPGs and other chemorepellents) benefited the success and growth rates of axonal regeneration the most. Physically, the CRMs-1 level was increased by increasing the seeding density of HA/LV-NT-3 and HA/LV-BDNF on the off-ramp of the scaffold, whereas the CRMs-2 level was reduced by increasing the seeding density of HA/LV-ChABC over the entire scaffold surface. However, raising the CRMs-3 (ECM components) level by increasing the density of HA/ECM components over the entire scaffold surface may create an over-eutrophic surface that harms axonal regeneration.

The theoretical predictions made in this study need to be experimentally validated in the future. In principle, the current tool can be easily modified for predictions regarding scaffolds with other architectures.

Author Contributions

Conceptualization: Weiping Zhu.

Data curation: Weiping Zhu.

Formal analysis: Kan Jin.

Investigation: Weiping Zhu, Han Zhang, Xuning Chen, Kan Jin, Le Ning.

Project administration: Weiping Zhu.

Software: Weiping Zhu, Le Ning.

Supervision: Weiping Zhu.

Validation: Weiping Zhu.

Writing – original draft: Weiping Zhu.

Writing – review & editing: Han Zhang, Xuning Chen, Kan Jin.

References

1. Fawcett JW, Asher RA. The glial scar and central nervous system repair. *Brain Res Bull.* 1999; 49: 377–391. PMID: [10483914](#)
2. Silver J, Miller JH. Regeneration beyond the glial scar. *Nat Rev Neurosci.* 2004; 5: 146–156. <https://doi.org/10.1038/nrn1326> PMID: [14735117](#)
3. Geller HM, Fawcett JW. Building a bridge: engineering spinal cord repair. *Exp Neurol.* 2002; 174: 125–136. <https://doi.org/10.1006/exnr.2002.7865> PMID: [11922655](#)
4. Zhang N, Yan H, Wen X. Tissue-engineering approaches for axonal guidance. *Brain Res Rev* 2005; 49:48–64. <https://doi.org/10.1016/j.brainresrev.2004.11.002> PMID: [15960986](#)
5. Li GN, Hoffman-Kim D. Tissue-engineered platforms of axon guidance. *Tissue Eng Part B Rev.* 2008; 14: 33–51. <https://doi.org/10.1089/teb.2007.0181> PMID: [18454633](#)
6. Fortun J, Hill CE, Bunge MB. Combinatorial strategies with Schwann cell transplantation to improve repair of the injured spinal cord. *Neurosci Lett.* 2009; 456: 124–132. <https://doi.org/10.1016/j.neulet.2008.08.092> PMID: [19429147](#)
7. Kim M, Park SR, Choi BH. Biomaterial scaffolds used for the regeneration of spinal cord injury (SCI). *Histol Histopathol.* 2014; 29: 1395–1408. <https://doi.org/10.14670/HH-29.1395> PMID: [24831814](#)
8. David S, Aguayo AJ. Axonal elongation into peripheral nervous system “bridges” after central nervous system injury in adult rats. *Science* 1981; 214: 931–933. PMID: [6171034](#)
9. Kanno H, Pressman Y, Moody A, Berg R, Muir EM, Rogers JH, et al. Combination of engineered Schwann cell grafts to secrete neurotrophin and chondroitinase promotes axonal regeneration and locomotion after spinal cord injury. *J Neurosci.* 2014; 34(5): 1838–1855. <https://doi.org/10.1523/JNEUROSCI.2661-13.2014> PMID: [24478364](#)
10. Hurtado A, Cregg JM, Wang HB, Wendell DF, Oudega M, Gilbert RJ, McDonald JW. Robust CNS regeneration after complete spinal cord transection using aligned poly-L-lactic acid microfibers. *Biomaterials* 2011; 32:6068–6079. <https://doi.org/10.1016/j.biomaterials.2011.05.006> PMID: [21636129](#)
11. Joo NY, Knowles JC, Lee GS, Kim JW, Kim HW, Son YJ, Hyun JK. Effects of phosphate glass fiber-collagen scaffolds on functional recovery of completely transected rat spinal cords. *Acta Biomaterialia* 2012; 8: 1802–1812. <https://doi.org/10.1016/j.actbio.2012.01.026> PMID: [22326790](#)
12. Lee JH, Lee JY, Yang SH, Lee EJ, Kim HW. Carbon nanotube–collagen three-dimensional culture of mesenchymal stem cells promotes expression of neural phenotypes and secretion of neurotrophic factors. *Acta Biomaterialia* 2014; 10: 4425–4436. <https://doi.org/10.1016/j.actbio.2014.06.023> PMID: [24954912](#)
13. Ahn HS, Hwang JY, Kim MS, Lee JY, Kim JW, Kim SH, et al. Carbon-nanotube-interfaced glass fiber scaffold for regeneration of transected sciatic nerve. *Acta Biomaterialia* 2015; 13: 324–334 <https://doi.org/10.1016/j.actbio.2014.11.026> PMID: [25463487](#)
14. Tuinstra HM, Margul DJ, Goodman AG, Boehler RM, Holland SJ, Zelivyanskaya ML. Long-term characterization of axon regeneration and matrix changes using multiple channel bridges for spinal cord regeneration. *Tissue Engineering Part A* 2014; 20: 1027–1037. <https://doi.org/10.1089/ten.TEA.2013.0111> PMID: [24168314](#)
15. Han S, Wang B, Jin W, Xiao Z, Li X, Ding W, et al. The linear-ordered collagen scaffold-BDNF complex significantly promotes functional recovery after completely transected spinal cord injury in canine. *Biomaterials* 2015; 41: 89–96. <https://doi.org/10.1016/j.biomaterials.2014.11.031> PMID: [25522968](#)
16. Liu C, Huang Y, Pang M, Yang Y, Li S, Liu L, et al. Tissue-engineered regeneration of completely transected spinal cord using induced neural stem cells and gelatin-electrospun poly (lactide-co-glycolide)/polyethylene glycol scaffolds. *PLoS One* 2015; <https://doi.org/10.1371/journal.pone.0117709> PMID: [25803031](#)
17. Chedly J, Soares S, Montebault A, von Boxberg Y, Veron-Ravaille M, Mouffle C, et al. Physical chitosan microhydrogels as scaffolds for spinal cord injury restoration and axon regeneration. *Biomaterials* 2017; 138: 91–107. <https://doi.org/10.1016/j.biomaterials.2017.05.024> PMID: [28554011](#)
18. Bunge MB. Novel combination strategies to repair the injured mammalian spinal cord. *J Spinal Cord Med.* 2008; 31: 262–269. PMID: [18795474](#)
19. Liu S, Sandner B, Schackel T, Nicholson L, Chtarto A, Tenenbaum L, et al. Regulated viral BDNF delivery in combination with Schwann cells promotes axonal regeneration through capillary alginate hydrogels after spinal cord injury. *Acta Biomaterialia* 2017; 60: 167–180 <https://doi.org/10.1016/j.actbio.2017.07.024> PMID: [28735026](#)
20. Houchin-Ray T, Swift LA, Jang JH, Shea LD. Patterned PLG substrates for localized DNA delivery and directed neurite extension. *Biomaterials* 2007; 28: 2603–2611. <https://doi.org/10.1016/j.biomaterials.2007.01.042> PMID: [17324456](#)

21. Hendriks WTJ, Eggers R, Verhaagen J, Boer GJ. Gene transfer to the spinal cord neural scar with lentiviral vectors: predominant transgene expression in astrocytes but not in meningeal cells. *J Neurosci Res.* 2007; 85: 3041–3052. <https://doi.org/10.1002/jnr.21432> PMID: 17671987
22. Laporte LD, Yan AL, Shea LD. Local gene delivery from ECM-coated poly(lactide-co-glycolide) multiple channel bridges after spinal cord injury. *Biomaterials* 2009; 30: 2361–2368. <https://doi.org/10.1016/j.biomaterials.2008.12.051> PMID: 19144400
23. Zhao RR, Muir EM, Alves JN, Rickman H, Allan AY, Kwok JC, et al. Lentiviral vectors express chondroitinase ABC in cortical projections and promote sprouting of injured corticospinal axons. *J Neurosci Methods* 2011; 201: 228–238. <https://doi.org/10.1016/j.jneumeth.2011.08.003> PMID: 21855577
24. Tuinstra HM, Aviles MO, Shin S, Holland SJ, Zelivyanskaya ML, Fast AG, et al. Multifunctional, multi-channel bridges that deliver neurotrophin encoding lentivirus for regeneration following spinal cord injury. *Biomaterials* 2012; 33: 1618–1626. <https://doi.org/10.1016/j.biomaterials.2011.11.002> PMID: 22130565
25. Boehler RM, Shin S, Fast AG, Gower RM, Shea LD. A PLG/HAp composite scaffold for lentivirus delivery. *Biomaterials* 2013; 34: 5431e5438.
26. Blesch A, Lu P, Tsukada S, Alto LT, Roet K, Coppola G. Conditioning lesions before or after spinal cord injury recruit broad genetic mechanisms that sustain axonal regeneration: superiority to campmediated effects. *Exp Neurol.* 2012; 235:162–173. <https://doi.org/10.1016/j.expneurol.2011.12.037> PMID: 22227059
27. Ruschel J, Hellal F, Flynn KC, Dupraz S, Elliott DA, Tedeschi A. Axonal regeneration systemic administration of epothilone B promotes axon regeneration after spinal cord injury, *Science* 2015; 348 (6232): 347–352. <https://doi.org/10.1126/science.aaa2958> PMID: 25765066
28. Hentschel HG, Ooyen AV. Models of axon guidance and bundling during development. *Proc R Soc B Biol Sci.* 1999; 266(1434): 2231–2238.
29. Ooyen AV. Using theoretical models to analyse neural development. *Nat Rev Neurosci.* 2011; 12: 311–326. <https://doi.org/10.1038/nrn3031> PMID: 21587288
30. Mortimer D, Feldner J, Vaughan T, Vetter I, Pujic Z, Rosoff WJ, et al. A Bayesian model predicts the response of axons to molecular gradients. *PNAS* 2009; 106(25):10296–10301. <https://doi.org/10.1073/pnas.0900715106> PMID: 19541606
31. Nguyen H, Dayan P, Pujic Z, Cooper-White J, Goodhill GJ. A mathematical model explains saturating axon guidance responses to molecular gradients. *eLife* 2016; 5: e12248. <https://doi.org/10.7554/eLife.12248> PMID: 26830461
32. Chen X, Zhu W. A mathematical model of regenerative axon growing along glial scar after spinal cord injury. *Computational and Mathematical Methods in Medicine* 2016; Article ID 3030454, 9 pages. <http://dx.doi.org/10.1155/2016/3030454>.
33. Sarvestani S A, Jabbari E. Analysis of Cell Locomotion on Ligand Gradient Substrates. *Biotechnol-Bioeng.* 2009; 103: 424–429.
34. Atzeni F, Sarzi-Puttini P, Bevilacqua M. Calcium deposition and dissociated chronic diseases (atherosclerosis, diffuse idiopathic skeletal hyperostosis, and others). *Rheum Dis Clin N Am.* 2006; 32: 413–426.
35. Tessier-Lavigne M, Goodman CS. The molecular biology of axon guidance. *Science* 1996; 274(5290): 1123–1133. PMID: 8895455
36. Dickson BJ. Molecular Mechanisms of Axon Guidance. *Science* 2002; 298(5600): 1959–1964. <https://doi.org/10.1126/science.1072165> PMID: 12471249
37. Rosoff WJ, Urbach JS, Esrick MA, McAllister RG, Richards LJ, Goodhill GJ. A new chemotaxis assay shows the extreme sensitivity of axons to molecular gradients. *Nat neurosci.* 2004; 7(6): 678–682. <https://doi.org/10.1038/nn1259> PMID: 15162167
38. Goodhill GJ. Diffusion in axon guidance. *Eur J Neurosci.* 1997; 9(7): 1414–1421. PMID: 9240399
39. Goodhill GJ. Mathematical guidance for axons. *Trends in Neurosci.* 1998; 21(6): 226–231.
40. Wensch J, Sommeijer B. Parallel simulation of axon growth in the nervous system. *Parallel Comput.* 2004; 30(2): 163–186.
41. Krottje JK, Ooyen AV. A mathematical framework for modeling axon guidance. *Bull Math Biol.* 2007; 69 (1): 3–31. <https://doi.org/10.1007/s11538-006-9142-4> PMID: 17061055
42. Bregman BS, Coumans JV, Dai HN, Kuhn PL, Lynskey J, McAtee M, Sandhu F. Transplants and neurotrophic factors increase regeneration and recovery of function after spinal cord injury. *Prog Brain Res.* 2002; 137(2):257–273.
43. GrandPré T, Nakamura F, Vartanian T, Strittmatter SM. Identification of the Nogo inhibitor of axon regeneration as a reticulon protein. *Nature* 2000; 403(6768): 439–444. <https://doi.org/10.1038/35000226> PMID: 10667797

44. Brittis P, Flanagan J. Nogo domains and a Nogo receptor implications for axon regeneration. *Neuron* 2001; 30(1): 11–14. PMID: [11343640](#)
45. Wang KC, Kim JA, Sivasankaran R, Segal R, He Z. P75 interacts with the Nogo receptors as a co-receptor for Nogo, MAG and OMgp. *Nature* 2002; 420(7): 74–78.
46. Tang BL. Inhibitors of neuronal regeneration: mediators and signaling mechanisms. *Neurochem Int.* 2003; 42(3): 189–203. PMID: [12427473](#)
47. Qian YH, Succi S, Orszag SA. Recent advances in lattice Boltzmann computing. *Ann Rev Comp Phys.* 1995; 10: 195–242.
48. Chen S, Doolen GD. Lattice Boltzmann method for fluid flows. *Ann Rev Flu Mech.* 1998; 30(5): 329–364.
49. Shi B, Deng B, Du R, Chen X. A new scheme for source term in LBGK model for convection-diffusion equation. *Comp Math Appl.* 2008; 55(7): 1568–1575.
50. Feng S, Zhu W. Bidirectional molecular transport shapes cell polarization in a two-dimensional model of eukaryotic chemotaxis. *J Theor Biol.* 2014; 363: 235–246. <https://doi.org/10.1016/j.jtbi.2014.08.033> PMID: [25167788](#)
51. McTigue DM, Horner PJ, Stokes BT, Gage FH. Neurotrophin-3 and brain-derived neurotrophic factor induce oligodendrocyte proliferation and myelination of regenerating axons in the contused adult rat spinal cord. *J Neurosci.* 1998; 18: 5354–5365. PMID: [9651218](#)
52. Sasaki M, Radtke C, Tan AM, Zhao P, Hamada H, Houkin K, et al. BDNF hypersecreting human mesenchymal stem cells promote functional recovery, axonal sprouting, and protection of corticospinal neurons after spinal cord injury. *J Neurosci.* 2009; 29: 14932–14941. <https://doi.org/10.1523/JNEUROSCI.2769-09.2009> PMID: [19940189](#)
53. Girard C, Bemelmans AP, Dufour N, Mallet J, Bachelin C, Nait-Oumesmar B, et al. Grafts of brain-derived neurotrophic factor and neurotrophin 3-transduced primate Schwann cells lead to functional recovery of the demyelinated mouse spinal cord. *J Neurosci.* 2005; 25: 7924–7933. <https://doi.org/10.1523/JNEUROSCI.4890-04.2005> PMID: [16135749](#)
54. Jain A, Kim YT, McKeon RJ, Bellamkonda RV. In situ gelling hydrogels for conformal repair of spinal cord defects, and local delivery of BDNF after spinal cord injury. *Biomaterials* 2006; 27: 497–504. <https://doi.org/10.1016/j.biomaterials.2005.07.008> PMID: [16099038](#)